Nanoscale

Modulating Phase by Metasurfaces with Gated Ultra-thin TiN Films

Journal:	*Nanoscale*
Manuscript ID	NR-ART-01-2019-000205.R1
Article Type:	Paper
Date Submitted by the Author:	15-Apr-2019

Complete List of Authors:	Jiang, Huan; Purdue University, Electrical and Computer Engineering ; Harbin Institute of Technology, Institute of Modern Physics Reddy, Harsha; Purdue University, School of Electrical and Computer Engineering Shah, Deesha; Purdue University, School of Electrical and Computer Engineering Kudyshev, Zhaxylyk ; Purdue University, School of Electrical and Computer Engineering Choudhury, Sajid; Purdue University, School of Electrical and Computer Engineering Wang, Di; Purdue University, School of Electrical and Computer Engineering Jiang, Yongyuan; Harbin Institute of Industry, Department of Physics Kildishev, Alexander; Purdue University, School of Electrical and Computer Engineering

SCHOLARONE™
Manuscripts

Please do not adjust margins

Nanoscale

ARTICLE

Modulating Phase by Metasurfaces with Gated Ultra-thin TiN Films

Received 00th January 20xx,
Accepted 00th January 20xx

DOI: 10.1039/x0xx00000x

www.rsc.org/

Huan Jiang,[a, b] Harsha Reddy,[b] Deesha Shah,[b] Zhaxylyk A. Kudyshev,[b] Sajid Choudhury,[b] Di Wang,[b] Yongyuan Jiang,*[a] and Alexander V. Kildishev*[b]

Active control over the flow of light is highly desirable because of its applicability to information processing, telecommunication, and spectroscopic imaging. In this paper, employing the tunability of carrier density in a 1-nm titanium nitride (TiN) film, we numerically demonstrate a deep phase modulation (PM) in an electrically tunable gold strip/TiN film hybrid metasurface. A 337° PM is achieved at 1.550 μm with a 3% carrier density change in TiN film. We also demonstrate that a continuous 180° PM can be realized at 1.537 μm by applying a realistic experiment-based gate voltage bias and continuously changing the carrier density in the TiN film. The proposed design of active metasurfaces capable of deep PM near the wavelength of 1.550 μm has considerable potential in active beam steering, dynamic hologram generation, and flat photonic devices with reconfigurable functionalities.

1. Introduction

In recent years, metasurfaces have enabled unprecedented capabilities to control light propagation, leading to major advances in a number of applications such as beam steering[1], focusing[2,3], hologram[4,5], polarization conversion[6,7], and cloaking[8]. However, these functionalities are achieved through careful engineering of phase fronts with static structures, and are remaining fixed at the point of fabrication. In contrast, dynamic light manipulation is in high demand, because with the active phase control, one can engineer a desired phase front in both space and time domains. The classical devices for dynamic PM rely on liquid crystals[9] and acousto-optic modulation[10], yet these modulators are relatively large and energy-inefficient. To address the limitations of these traditional methods, there has been a large effort to design active PM metasurfaces using a variety of alternative material platforms, including phase change (vanadium dioxide, VO_2)[11], semiconductor (gallium arsenide, GaAs)[12], two dimensional (graphene)[13–16], and transparent conducting oxide (indium tin oxide, ITO)[17,18] materials. A 60° PM based on VO_2 phase transition has been demonstrated at 10.6 μm[11], but the phase transition occurs over a long-time scale (ms) resulting in a slow modulation[19]. To achieve faster PM, graphene-integrated metasurfaces are explored to electrically control phase in the mid-IR region[13–15], among which a PM exceeding 230° has been demonstrated experimentally[16]. Also, ITO-based phase modulators capable of deep phase control work not only in the mid-IR[17], but also in the telecom bands[18], broadening the wavebands of dynamic PM. However, the visible and near-infrared spectral regions are of the utmost importance for sensing and optical signal processing technologies, so the development of active metasurfaces is still in great importance at these wavelengths.

Ultra-thin metal films have emerged as promising materials to realize tunable nanophotonic devices due to their sensitivity to external electrical and optical perturbations[20]. In contrast to bulk metals, the optical properties of atomically thin materials can be tailored by altering the composition and the thickness during the thin film growth process[21,22]. While noble metals (Au, Ag) are incompatible with existing semiconductor fabrication process, preventing the practical realization of on-chip, CMOS-compatible applications[23], transition metal nitrides with a high melting point become good candidates for tailorable ultra-thin plasmonic devices[24]. Also, the epitaxial growth of titanium nitride (TiN) on c-sapphire and magnesium oxide (MgO) substrates[25] has facilitated the experimental demonstration of ultrathin plasmonic films that maintain high metallicity[21,22,26]. The high-quality growth and tailorable optical response establish ultrathin TiN as an attractive material platform to design electrically tunable plasmonic devices operating in the visible and near-infrared wavelength ranges.

Here, we study the tunability of carrier density in a 1-nm TiN film and numerically demonstrate an Au strip-TiN film hybrid metasurface (ATHM) for deep PM at the telecom band. While the ultra-thin TiN film remains highly metallic with a carrier density on the order of 10^{22} cm^{-3}, the carrier density in ultra-thin TiN film can be efficiently modulated up to 12% by using a conventional electric gating technology with a switching time of nanoseconds. The proposed ATHM achieves the deep 337°

[a] Institute of Modern Optics, Department of physics, Harbin Institute of Technology, Harbin 150001, China
[b] School of Electrical and Computer Engineering and Birck Nanotechnology Center, Purdue University, West Lafayette, Indiana 47907, United States
*Corresponding authors' emails: kildishev@purdue.edu; jiangyy@hit.edu.cn.

Please do not adjust margins

PM at 1.550 μm by reducing the TiN carrier density by only 3%. Additionally, a monotonic phase change along with decreasing TiN carrier density predicts a continuous 180° PM at 1.537 μm. The proposed PM metasurface consists of an Au strip array on top of a 1-nm TiN film, and the Au strip-TiN film structure is placed on a 150-nm Au underlayer separated by a 45-nm Al_2O_3 spacer layer as schematically shown in Fig. 1(a). Due to the Au underlayer, the reflection can be qualitatively understood by the modelling system as one-port resonators within the framework of coupled mode theory (CMT)[14,17,27]. The one-port CMT model assumes that incident light polarized along the x axis (see Fig. 1(a)) can be reflected from the metasurface through two channels: a non-resonant channel and a resonant scattering channel (the reflections of the incident waves polarized along other directions are discussed later). For the non-resonant channel, the Au underlayer acts as a high-impedance mirror, which produces a reflection r_{nr} with amplitude $r_{nr,0}$ and a certain reflection phase θ_{nr} (the subscript nr denotes non-resonant). For the resonant scattering channel, upon illumination with x-polarized light, the resonators support the gap plasmon mode as magnetic resonators. The localized electric field outside the Au strips (Fig. 1(b)) and the highly confined magnetic field inside the dielectric spacer (Fig. 1(c)) demonstrate the magnetic resonance mode. The reflection coefficient through the resonant scattering channel is described as $r_r = r_{r,0}\exp(i\theta_r)$, where the subscript r denotes resonant. The destructive interference between the reflected light from the two channels contributes to the total reflection $r_{tot} = r_{nr}+r_r$. When the reflection from both channels have almost the same amplitudes ($r_{nr,0} \cong r_{r,0}$) with an abrupt phase increase across the resonant wavelength, the critical coupling (CC) state is achieved. This CC state features a near-zero total reflection at the resonant wavelength and a 180° phase jump across the resonant wavelength. Thus, the period, the width of Au strips and the thickness of the dielectric spacer of the proposed metasurface are optimized to achieve the CC state at the 6% lower TiN carrier density from the unperturbed value. (The reflections with varying geometric parameters are outlined in the Supporting Information). The reflection coefficient and phase of the ATHM at the CC state are plotted in Figs. 1(d)(e), where the total reflection coefficient is near zero as shown in Fig. 1(d), and the total reflection phase experiences 180°phase jump across the wavelength of 1.540 μm (Fig. 1 (e)).

2. Structure design and operation principles

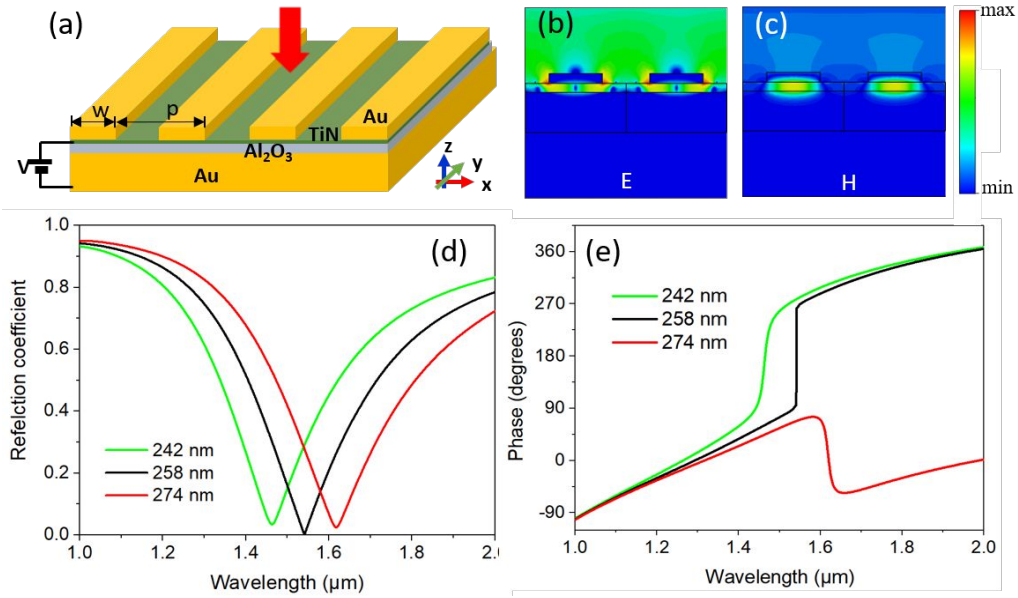

Fig. 1 PM by tuning geometric parameters. (a) Schematic of ATHM. The width, period and the thickness of Au strips are *w* = 258 nm, *p* = 500 nm, and 50 nm, respectively. The thickness of the TiN film and Al2O3 spacer are 1 nm and 45 nm, respectively. Tangential electric (b) and magnetic (c) field distributions in x-z plane at the resonant wavelength of 1.540 μm. Reflection coefficients (d) and phases (e) with different widths of Au strips at 6% lower TiN carrier density (9.4×10^{21} cm^{-3}) from its unperturbed value (10^{22} cm^{-3}).

Additionally, the balance between the two channels can be broken by either enhancing or diminishing the gap plasmon mode (magnetic resonance). We tune the reflection in resonant scattering channel by changing the width of Au strips to be either smaller or greater than the reflection in the non-resonant channel, and thereby modulate the reflection phase by moving in and out of the CC state. The CC state moves into an over-coupling (OC) state when the reflection of the resonant scattering channel becomes greater than that of the non-resonant channel ($r_{r,0} > r_{nr,0}$) at the resonant wavelength. Otherwise, the under-coupling (UC) state is established when non-resonant scattering channel is dominant ($r_{r,0} < r_{nr,0}$). The OC state is achieved by reducing the width of the Au strips to 242 nm while UC state is obtained using wider strips of 274 nm. As a result, the total reflection coefficient of both OC and UC states are larger than the CC state at their corresponding resonant wavelengths as shown in Fig. 1(d). On the other hand, in Fig. 1(e), the phase of the OC state across the

This journal is © The Royal Society of Chemistry 20xx

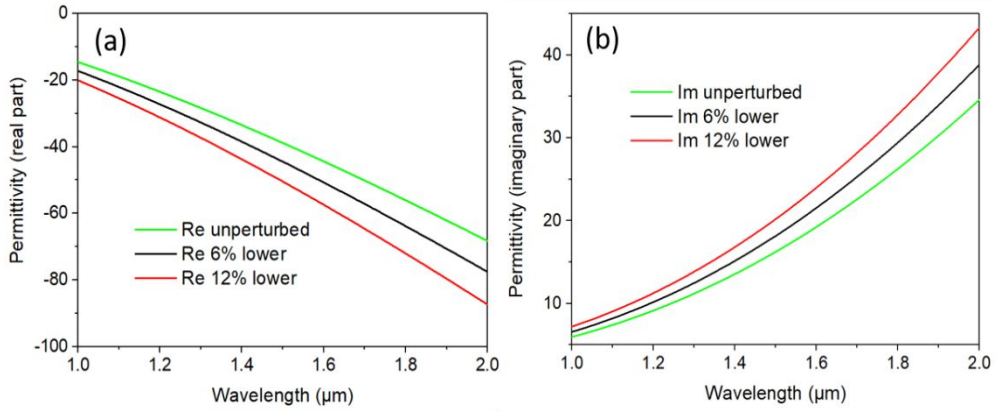

Fig. 2 The (a) real and (b) imaginary parts of the permittivity of 1-nm TiN film with varying carrier densities.

resonant wavelength of 1.475 μm (green curve) experience slower increase than that of the CC state across 1.540 μm (black curve), while the phase of UC state (red curve) decreases less 180° across the resonant wavelength of 1.623 μm. Due to the differences in the reflection phases among the three coupling states, the PM is achieved at a certain wavelength by tuning the Au strip width. In addition to the geometry, the material parameters also affect the coupling state. In the next section, we numerically demonstrate that the relative contributions of the two channels can be manipulated by tuning the carrier density of the TiN film.

3. Deep phase modulation via electrical control

Figure 2 depicts the estimated permittivity for varying carrier densities in a 1-nm TiN film. We use the experimentally retrieved permittivity of the ultra-thin TiN film[21] and estimate the carrier density-dependent permittivity of a 1-nm film by changing the plasma frequency as:

$$\omega_p^2 = \frac{N_0(1+\frac{\Delta N}{N_0})e^2}{m^*\varepsilon_0} \quad (1)$$

where N_0 is the unperturbed free electron density and $\Delta N/N_0$ is the relative change in the carrier density, while m^* and ε_0 represent the electron effective mass and the permittivity of free space respectively. A Drude-Lorentz model consisting of one Drude oscillator and one Lorentz oscillator is used to estimate the permittivity[21]

$$\varepsilon(\omega) = \varepsilon_\infty - \frac{\omega_p^2}{\omega^2 + i\Gamma_D\omega} + \frac{f_L\omega_L^2}{\omega_L^2 - \omega^2 - i\Gamma_L\omega} \quad (2)$$

where ε_∞ is the permittivity at high frequency, ω_p is the plasma frequency, f_L is the strength of the Lorentz oscillator, ω_L is the resonant frequency of the Lorentz oscillator, and Γ_L and Γ_D are the damping rates of the oscillators. The Drude term captures the optical response of the free carriers, while the Lorentz term accounts for interband transitions. We calculated the reflection coefficient and phase spectra of the ATHM with different carrier densities using frequency domain solver base on a finite element method in a 3D electromagnetic simulation Software (CST). The boundary conditions are periodic in x and y directions, and open for ±z direction in free space. The complex permittivity of Au[28] and 50-nm Al_2O_3 spacer are experimentally obtained (see the Supporting Information).

By changing the carrier density in TiN film, the proposed metasurface can be tuned from OC to UC state, similar to the switching behavior demonstrated with the changing of Au strip width shown in Figs. 1(d) and (e). To design our dynamic phase modulator, we reduce the carrier density in the 1-nm TiN film by up to 12%, a number experimentally achievable with existing gating approaches[20]. The calculated reflection coefficient and phase of the optimized structure with the TiN carrier density reduced by 6% and 12% from the unperturbed value ($10^{22}cm^{-3}$) are shown in Figs. 3(a) and (b). As the TiN carrier density decreases, the reflection dip displays a slight blueshift as shown in Fig. 3(a). The near-zero reflection coefficient and 180° phase jump at 1.540 μm in Figs. 3(a)(b) represent the CC state of the optimized structure at 6% lower carrier density. The reflection coefficients with the unperturbed and 12% lower carrier density are both larger than the

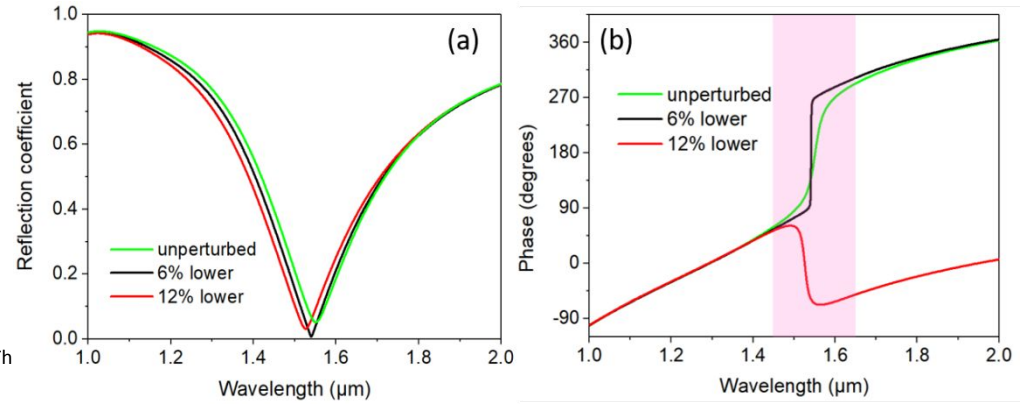

Fig.3 PM by tuning the carrier density in TiN film. Reflection coefficient (a) and phase (b) with different carrier densities of 1-nm TiN film.

6% lower case at their corresponding resonant wavelengths, which demonstrates the breaking of balance between the resonant scattering channel and non-resonant channel. By increasing the TiN carrier density to the unperturbed value, the CC state of the ATHM moves into an OC state, and the phase increases more slowly across 1.552 μm (green curve in Fig. 3(b)). By decreasing the TiN carrier density to the 12% lower value, the metasurface moves into the UC state (red curve) and displays a 129°
phase decrease across the wavelength of 1.526 μm. Therefore, gating the ultra-thin TiN film allows switching among different coupling states, and dynamically modulating the reflection phase at certain wavelengths.

To better understand the nature of the deep PM, in Fig. 4(a) we focus on the reflection phases of the three TiN carrier densities in the waveband from 1.45 μm to 1.65 μm (marked by the pink area in Fig. 3(b)). The phase with the 6% lower carrier density allows 180° phase jump from 90° to 270° across the resonant wavelength of 1.540 μm. The phase with the 9% lower carrier density decreases by 140° across the resonant wavelength of 1.536 μm. A relative phase difference of approximately 337° is observed at 1.550 μm by reducing the TiN carrier density by 3% from the 6% lower carrier density value as shown in Fig. 4(b) (at the wavelength marked by a dashed blue line in Fig. 4(a)). Additionally, the reflection phase increases more and more slowly across the resonant wavelength with the carrier density increasing from 6% lower to unperturbed values. With the carrier density decreasing from 9% lower to 12% lower values, the phase decreases more slowly too. Thus at 1.537 μm (dashed black line marked in Fig. 4(a)) a continuous 180° PM can be realized by decreasing the TiN carrier density by up to 12% in Fig. 4(c). The PM at 1.550 μm and 1.537 μm manifest the difference directly in the relative contribution between the resonant scattering and the non-resonant channels.

To further understand the differences among OC, CC, and UC states, we plot the complex reflection coefficients at the waveband from 1.3 μm to 2 μm for three TiN carrier densities on a Smith chart (polar plot) in Fig. 4 (d). Analysis based on CMT showed that the reflection coefficient r_{tot} of such a system can be generally expressed as [14,17,27]

$$r_{tot} = \frac{(\gamma_{rad} - \gamma_{abs}) - i(\omega - \omega_0)}{(\gamma_{rad} + \gamma_{abs}) + i(\omega - \omega_0)} \quad (3)$$

Where γ_{abs} and γ_{rad} respectively represent the losses from non-resonant channel and resonant scattering channel, while ω and ω_0 are the angular frequency and the resonance angular frequency. The evolution of r_{tot} is reflected in the Smith chart, which traces r_{tot} on the complex plane as ω increases from 0 to ∞. The relative amplitudes of γ_{abs} and γ_{rad} govern the behaviour of the reflection phase. At $\gamma_{rad} < \gamma_{abs}$, the reflection spectra for the CC state cover the first and fourth quadrants of the complex plane almost passing through the origin, which demonstrates the 180° phase jump from 90° to 270° across 1.540 μm. At $\gamma_{rad} > \gamma_{abs}$, the reflection spectra on OC state cover four quadrants with the slower phase increase than

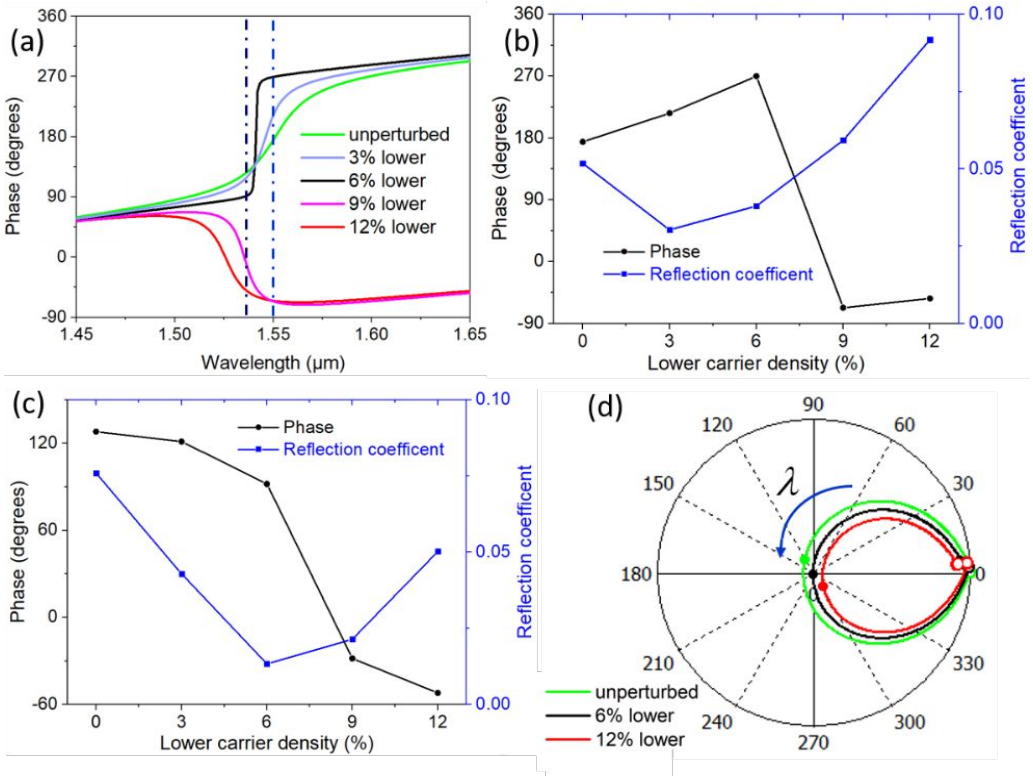

Fig. 4 Deep PM at certain wavelengths. (a) Reflection phase spectra for different carrier densities of TiN film. Reflection phases and coefficients at (b) 1.550 μm and (c) 1.537 μm, respectively. (d) Polar plot of complex reflection coefficients for varying carrier densities of TiN. The three counter-clockwise trajectories of complex reflection coefficients with the wavelength increasing from 1.3 μm to 2 μm represent three coupling states: UC (red curve), CC (black curve), and OC (green curve).

This journal is © The Royal Society of Chemistry 20xx

the CC state at the same waveband. At $\gamma_{rad} < \gamma_{abs}$, for the UC state, the reflection spectra follow a trajectory located in the first and fourth quadrants of the complex plane, displaying less than 180° phase decrease across 1.526 µm. Specifically, the three solid points on reflection curves in Fig. 4(d) predict the continuous PM at 1.537 µm. Decreasing the TiN carrier density by 12% results in a 180° PM from 127° (solid green dot) to -53° (solid red dot). As observed in the Smith chart, the position of the solid dot, which represents the phase at 1.537 µm, passes through the CC state (solid black dot) when reducing the carrier density from the unperturbed state by 12%. Thus, the continuous PM within 180° phase range from 127° to -53° can be realized by keeping the reflection in the line between the green and red dots.

4. Polarization angle-dependent PM

The PM depends on the polarization direction of the incident light, because the gap plasmon mode can only be excited by light polarized orthogonally to the Au strips ($\theta = 90°$), resulting in near-zero reflection at the resonant wavelength of 1.540 µm and 180° phase jump across resonant wavelength as shown with the dashed black curves in Figs. 5(a) and (b). For the incident light polarized parallel to the Au strips ($\theta = 0°$), our metasurface acts as a perfect electric conductor with the near-unit reflection coefficient as shown with the solid black line in Fig. 5(a). The magnitude of the reflection decreases, and the covered phase range increases with increasing polarization angle (see Figs. 5(a) and (b)). These changes in reflection coefficient happen because the x-component of incident light increases as the polarization angle varies from 0° to 90°. Since the magnitude of the reflection coefficient is extremely small at 90° polarization angle, the reflection coefficient and phase at a given angle can be extracted from measured reflection intensity at a set of incident angles (discussed in the Supporting Information).

5. Conclusions

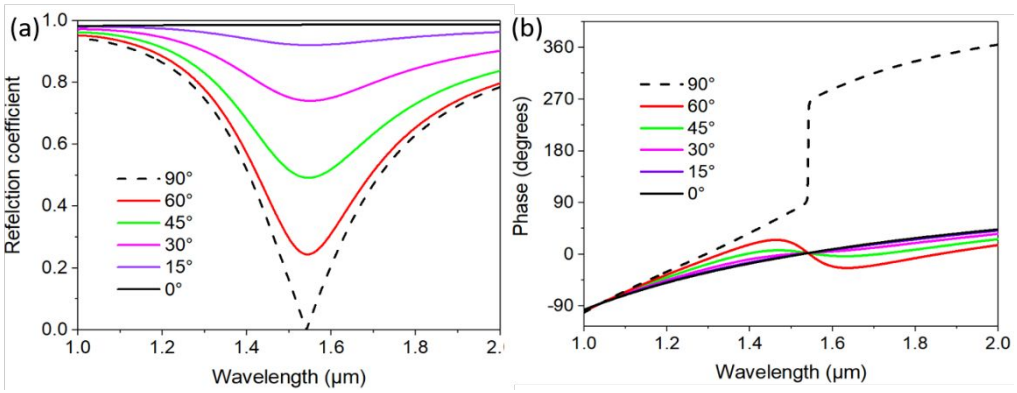

Fig. 5 Polarization-dependent PM. The (a) reflection coefficients and (b) phases with various incident polarization angles. The polarization angle (θ) is defined as the angle between polarized direction and Au strips (y axis).

In summary, an ultra-thin TiN based metasurface with deep PM is designed by balancing the contributions between the non-resonant and the resonant scattering channels within the framework of coupled mode theory. The realized dynamic metasurface design enables 337° PM at 1.550 µm, which is achieved by using realistic experiment-based numbers for carrier density changes in the 1-nm TiN film. Based on these results we conclude that the ultra-thin TiN film, an emerging electrically-tunable material, offers an alternative material platform for realizing dynamic light manipulation in the visible and near-IR wavelength ranges. Therefore, the demonstrated electrically tunable PM, which relies on controlling the optical properties of the ultra-thin TiN film, offers novel approaches towards the realization of innovatory active metasurface devices.

Acknowledgements

The authors acknowledge the financial support by DARPA/DSO Extreme Optics and Imaging (EXTREME) Program (HR00111720032) and China Scholarship Council (CSC).

References

1 X. Ni, N. K. Emani, A. V. Kildishev, A. Boltasseva and V. M. Shalaev, *Science*, 2012, **335**, 427.
2 M. Khorasaninejad, W. T. Chen, R. C. Devlin, J. Oh, A. Y. Zhu and F. Capasso, *Science*, 2016, **352**, 1190–1194.
3 A. Pors, M. G. Nielsen, R. L. Eriksen and S. I. Bozhevolnyi, *Nano Lett.*, 2013, **13**, 829–834.
4 X. Ni, A. V. Kildishev and V. M. Shalaev, *Nat. Commun.*, 2013, **4**, 1–6.
5 W. Zhao, H. Jiang, B. Liu, J. Song, Y. Jiang, C. Tang and J. Li, *Sci. Rep.*, 2016, **6**, 30613.
6 W. T. Chen, K. Y. Yang, C. M. Wang, Y. W. Huang, G. Sun, I. Da Chiang, C. Y. Liao, W. L. Hsu, H. T. Lin, S. Sun, L. Zhou, A. Q. Liu and D. P. Tsai, *Nano Lett.*, 2014, **14**, 225–230.
7 Y. Zhao and A. Alu, *Nano Lett.*, 2013, **13**, 1086–1091.
8 D. Schurig, J. J. Mock, B. J. Justice, S. A. Cummer, J. B. Pendry, A. F. Starr and D. R. Smith, *Science*, 2006, **314**, 977–980.
9 D. P. Resler, D. S. Hobbs, R. C. Sharp, L. J. Friedman and T. A. Dorschner, *Opt. Lett.*, 1996, **21**, 689–691.
10 S.-H. Shim, D. B. Strasfeld, E. C. Fulmer and M. T. Zanni, *Opt. Lett.*, 2006, **31**, 838–840.
11 D. J. Shelton, K. R. Coffey and G. D. Boreman, *Opt. Express*, 2010, **18**, 1330–1335.
12 Y. C. Jun, J. Reno, T. Ribaudo, E. Shaner, J.-J. Greffet, S. Vassant, F. Marquier, M. Sinclair and I. Brener, *Nano Lett.*, 2013, **13**, 5391–5396.

13 N. Dabidian, S. Dutta-Gupta, I. Kholmanov, K. Lai, F. Lu, J. Lee, M. Jin, S. Trendafilov, A. Khanikaev, B. Fallahazad, E. Tutuc, M. A. Belkin and G. Shvets, *Nano Lett.*, 2016, **16**, 3607–3615.
14 Z. Miao, Q. Wu, X. Li, Q. He, K. Ding, Z. An, Y. Zhang and L. Zhou, *Phys. Rev. X*, 2015, **5**, 1–13.
15 Y. Zhang, Y. Feng, B. Zhu, J. Zhao and T. Jiang, *Opt. Express*, 2014, **22**, 22743.
16 M. C. Sherrott, P. W. C. Hon, K. T. Fountaine, J. C. Garcia, S. M. Ponti, V. W. Brar, L. A. Sweatlock and H. A. Atwater, *Nano Lett.*, 2017, **17**, 3027–3034.
17 J. Park, J. H. Kang, S. J. Kim, X. Liu and M. L. Brongersma, *Nano Lett.*, 2017, **17**, 407–413.
18 G. Kafaie Shirmanesh, R. Sokhoyan, R. A. Pala and H. A. Atwater, *Nano Lett.*, 2018, **18**, 2957–2963.
19 J. Yoon, H. Kim, X. Chen, N. Tamura, B. S. Mun, C. Park and H. Ju, *ACS Appl. Mater. Interfaces*, 2016, **8**, 2280–2286.
20 A. Manjavacas and F. J. García de Abajo, *Nat. Commun.*, 2014, **5**, 3548.
21 D. Shah, H. Reddy, N. Kinsey, V. M. Shalaev and A. Boltasseva, *Adv. Opt. Mater.*, 2017, **5**, 1–5.
22 D. Shah, A. Catellani, H. Reddy, N. Kinsey, V. Shalaev, A. Boltasseva and A. Calzolari, *ACS Photonics*, 2018, **5**, 2816–2824.
23 A. Boltasseva and H. A. Atwater, *Science*, 2011, **331**, 290–291.
24 H. Reddy, U. Guler, Z. Kudyshev, A. V. Kildishev, V. M. Shalaev and A. Boltasseva, *ACS Photonics*, 2017, **4**, 1413–1420.
25 G. V Naik, J. L. Schroeder, X. Ni, A. V Kildishev, T. D. Sands and A. Boltasseva, *Opt. Mater. Express*, 2012, **2**, 478–489.
26 G. V. Naik, B. Saha, J. Liu, S. M. Saber, E. A. Stach, J. M. K. Irudayaraj, T. D. Sands, V. M. Shalaev and A. Boltasseva, *Proc. Natl. Acad. Sci.*, 2014, **111**, 7546–7551.
27 S. Fan and W. Suh, 2003, **20**, 569–572.
28 H. Reddy, U. Guler, A. V Kildishev, A. Boltasseva and V. M. Shalaev, *Opt. Mater. Express*, 2016, **6**, 2776–2802.

This journal is © The Royal Society of Chemistry 20xx